An improved distortion compensation approach for additive manufacturing using optically scanned data

Shukri Afazov [a*], Eleonora Semerdzhieva [b], Daniele Scrimieri [c], Ahmad Serjouei [a], Bekmurat Kairoshev [d], Fatos Derguti [d]

[a] Department of Engineering, Nottingham Trent University, Clifton Campus, Nottingham, NG11 8NS, UK

[b] AXIMEL Ltd, Nottingham, NG9 1GN, UK

[c] Department of Computer Science, University of Bradford, Bradford, BD7 1DP, UK

[d] 3T Additive Manufacturing Ltd, Fulton Court Greenham Business Park, Greenham, Thatcham, RG19 6HD, UK

*corresponding author (shukri.afazov@ntu.ac.uk)

Abstract

This paper presents an improved mathematical model for calculation of distortion vectors of two aligned surface meshes. The model shows better accuracy when benchmarked to an existing model with exceptional mathematical conditions, such as sharp corners and small radii. The model was implemented into a developed distortion compensation digital tool and applied to an industrial component. The component was made of Inconel 718 and produced by laser powder bed fusion 3D-printing technology. The digital tool was utilised to compensate the original design geometry by pre-distortion of its original geometry using the developed mathematical model. The distortion of an industrial component was reduced from approximately ±400µm to ±100µm for a challenging thin structure subjected to buckling during the build process.

Keywords: distortion compensation; mathematical modelling; geometric predistortion; additive manufacturing; 3D-printing

1. Introduction

Additive manufacturing (AM) represents a large number of processes covering a wide range of materials. For many of the AM processes, the material is deposited layer-by-layer. Metals are processed based on the principle of melting or sintering the material. The material for a wide range of AM processes is in the form of a powder. The melting is achieved by applying a heat source (i.e laser or electron beam) which melts the powder and builds the physical part (King et al., 2015). The workflow for AM includes the following digital steps. The design for additive manufacturing (DfAM) of functional industrial parts involves the use of computer-aided design (CAD) algorithms and functionalities for the creation of a digital representation of the physical object which will be additively manufactured. The AM constraints should be considered in the design stage. For example, in laser

powder bed fusion (L-PBF) and other metal AM processes, the overhang should be less than 45° to prevent the use of supports (Garaigordobil et al., 2019). The next step is to create a scan path for the laser with a set of instructions for the location of the laser, its speed and power input. The scan path is created by slicing the geometry. Slicing the CAD could represent difficulties due to the complexity of mathematical functions used, including splines and NURBS (Bracco et al., 2018). To reduce the complexity in slicing, a surface meshing is used to represent the surfaces of the geometry. A common practice is to use stereolithography (STL) format which is a representation of a surface mesh with triangular elements. Support structures are modelled if required. The machine volume and reference coordinate system is selected. The slicing is then applied to the STL mesh using mathematical algorithms (Steuben et al., 2016). Once the geometric object is sliced, the scan path is generated by applying scanning strategies. The instruction code is then generated to move the laser in space with a velocity and a specified power. Once all instructions are completed by the machine, the physical part is 3D-printed.

One of the key challenges in metal AM is that the parts distort during the build process which might affect their performance in terms of designed functionalities (Chahal and Taylor, 2020). In addition, distorted part might not fit within a system due to dimensional tolerances. Researchers have used the approach of applying greater amount of support structures to increase the geometrical stiffness and reduce distortion (Jiang et al., 2018). Eisenbarth et al. (2019) have suggested to add stock material which can be milled as a possible solution for mitigation of distortion in direct energy deposition (DED). However, this approach increases the waste and cost of the print through increasing the amount of printed material (Thomas-Seale et al., 2018). Pre-distortion of the geometry is another approach to address the distortion problem of printed parts. Pre-distortion of simple in shape geometries have been approached with analytical methods. For instance, Huang et al. (2015) developed a theoretical framework for optimal deformation compensation of 3D shapes through a minimum volume deviation criterion. Cheng et al. (2018) proposed a two-stage analytical method for in-plane distortion mitigation of 2D geometries and validated it against experiments. However, their method still needs to be extended to be applicable to 3D geometries. Xu et al. (2017) proposed a method for distortion compensation in which measurements on the fabricated nominal and offset models are needed to calculate the required pre-distortion. Afazov et al. (2017a) used optically scanned data to compensate the geometry represented by a surface mesh. They demonstrated that the concept of applying pre-distortion to reduce the distortion in L-PBF of an impeller and a blade made of Inconel 718. They also suggested that computer tomography (CT) scan could be also used in addition to the optical scans. Afazov at al. (2017b) and Yaghi et al. (2019) used finite element-based approaches to compensate the distortion of industrial components made of L-PBF. Biegler et al. (2020) used a transient finite element thermal model coupled with mechanic analyses to predict distortion and compensated for the DED process. The main challenge with the finite element-based approach is that for some geometries and metal alloys with complex material composition and presence of phase changes, the modelling complexity can increase, leading to challenges in the accurate prediction of residual stresses and distortion. The commercially offered distortion compensation toolkits are based on the finite element approach (e.g. ANSYS Additive, Netfabb Simulation, Simufact Additive, Additive Works). Despite the trend of the development of physics-based predictive finite element models for residual stress and distortion compensation by the software vendors, this paper presents a data-driven mathematical approach to deliver the distortion compensation in additive manufacturing. As the data-driven approach uses measured data, the method is applicable to any additive manufacturing process and material without the need of inputs for the physics-based models. This is a significant benefit in industry, as the method does not require to model the specific physics for the additive manufacturing process and material. This advantage makes the approach easier to apply to any process, material and geometry. However, errors due to measurements and calculations can accumulate and, therefore, they need to be controlled and kept to a minimum.

This paper aims to advance the mathematical model for distortion calculation presented in Afazov et al. (2017a) in order to deliver more accurate distortion compensation, particularly in sharp and rounded corners as well as when the surface meshes are created with large transition of large to small elements or vice versa. This is a very common case for many of the commercial software packages available for build preparation.

This work compares two mathematical models: the first one, surface method (S-method), is the model developed by Afazov et al. (2017a) with an advanced criterion for element detection proposed in this study, while the second one, hybrid method (H-method), is an improved model proposed in this paper, which is the novelty in this paper. The two models are benchmarked against exceptional mathematical conditions which are common for many industrial geometries with complex surfaces and features. The improved mathematical model is then applied to an industrial component, made of Inconel 718 and produced by L-PBF, to demonstrate the feasibility of distortion compensation.

2. Distortion compensation - a concept

In AM as well as in manufacturing as a whole, the desirable outcome is that the designed parts are produced within required tolerances. In metal AM, the parts distort due to the induced residual stresses. Researchers have studied the residual stresses on Inconel 718 (Papadakis et al., 2014), stainless steel 316L (Saboori et al., 2020; Liu et al., 2016), AlSi10Mg (Salmi et al., 2018) and steel (Li et al., 2016). Figure 1 illustrates a distortion compensation concept where a designed geometry is manufactured using metal AM. The geometry after manufacturing is distorted which do not satisfy the required tolerances. In many industrial applications, distortion in complex geometrical shapes is measured by optically scanning the part using white or blue light technologies (Martinez-Pellitero et al., 2018). The intention in distortion compensation is to pre-distort the original designed geometry such that when the pre-distorted geometry is manufactured, the final measured geometry is close in dimensions to the original designed geometry.

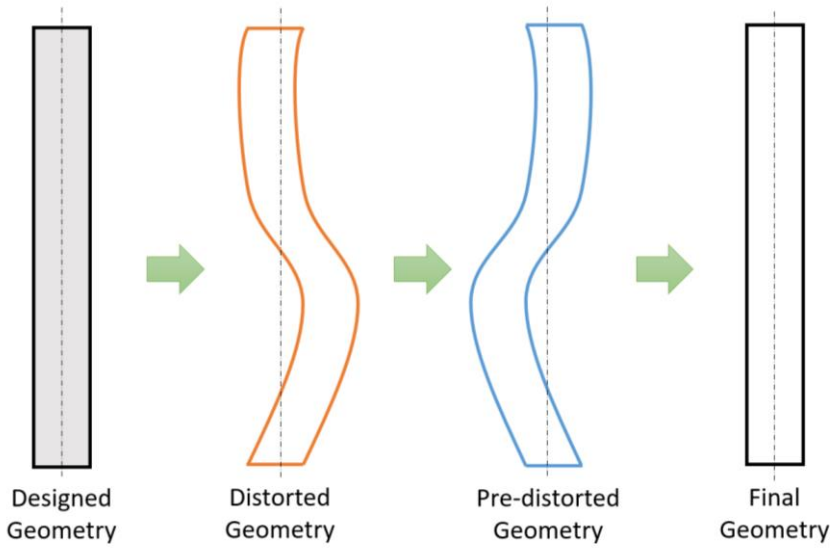

Figure 1 Distortion compensation concept

The key step in the distortion compensation process is how to pre-distort the geometry. In AM, the original designed geometry is represented by a surface mesh in STL format. This means that the pre-distortion can be achieved by changing the coordinates of the STL mesh. To achieve this, the displacement vectors need to be computed. The first step is to align the original designed geometry to the distorted geometry (see Figure 2). For each measured point from the distorted geometry, the displacement vectors need to be calculated. Once all vectors are calculated, the nodes are inverted by

changing the coordinates of the measured points. This is how the measured geometry can be pre-distorted.

In practice, the optically scanning technologies cannot access all surfaces of industrial parts. For instance, internal surfaces could not be scanned because the light cannot reach them. The displacement vectors are calculated on the measured points followed by an interpolation to map the calculated displacement vectors onto a surface mesh representing the original designed geometry. Once the mapping step is done, the coordinates of the surface mesh are updated by inverting the displacement vectors and changing the coordinate. For example, if a node from the surface mesh has coordinates in x, y, and z direction (100, 50, 10) and the mapped displacement vectors in x, y and z directions are (0.5, -0.2, -0.8), the updated coordinates of that node will be (99.5, 50.2, 10.8). The mapping can be done using interpolation techniques. The method using field of points is used in this study (Afazov et al., 2012).

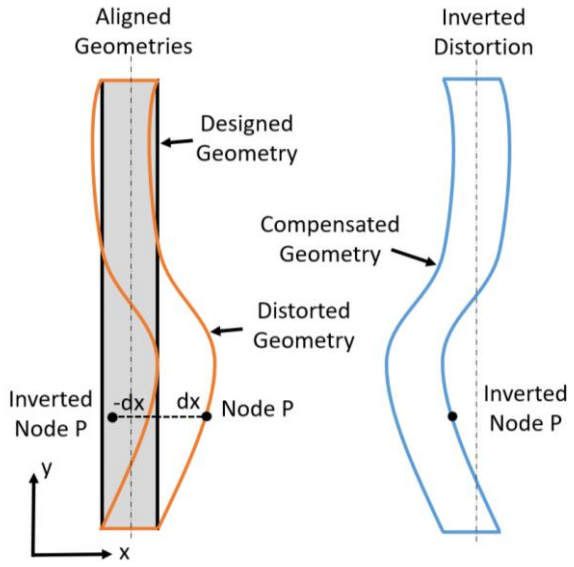

Figure 2 Distortion inversion concept

2. Mathematical models for distortion calculation and inversion

2.1 Distortion inversion

The raw 3D optical scanning measurement data is represented as a surface mesh with triangular elements defined by three nodes. This surface mesh is referred to as distorted surface mesh. Figure 3 shows three nodes (A, B and C) representing an element from the original designed surface mesh, while node P is a node from the distorted surface mesh.

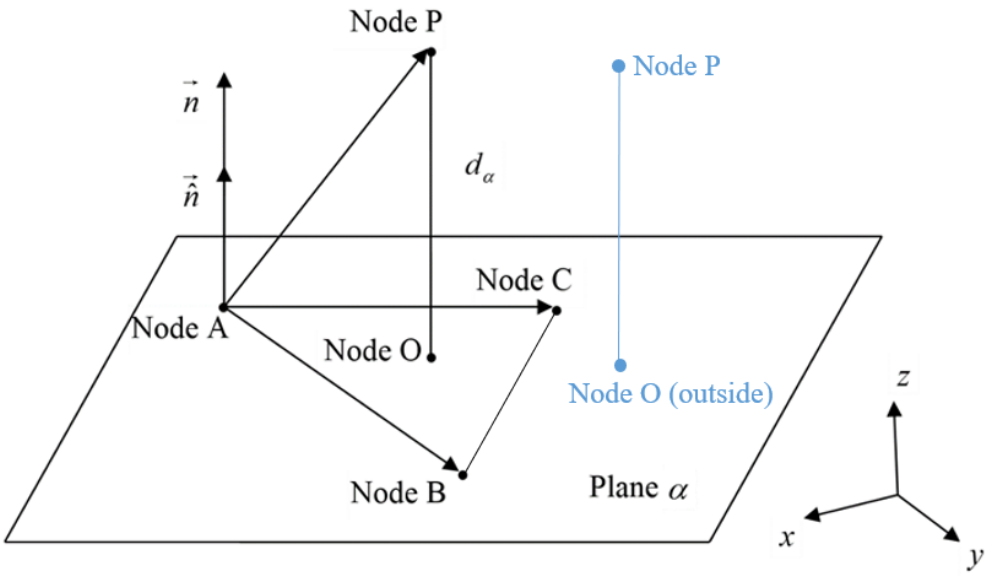

Figure 3 A schematic description of the mathematical model. Note that the notations in blue show a scenario where node O, which is the projection of node P, is located outside the triangle ABC.

The key task is to identify to which element from the original designed surface mesh the projection of Node P (denoted Node O in Figure 3) belongs, in order to invert the coordinates of Node P in the opposite direction of the Plane α (Afazov et al., 2017a). The position of Node P is checked relative to all elements of the original designed surface mesh using a search algorithm with indexing described in section 4.

The direction vectors $\overrightarrow{AB}$, $\overrightarrow{AC}$ and $\overrightarrow{AP}$ can be calculated from the coordinates of nodes A, B, C and P from the distorted and original designed surface meshes by:

$$\overrightarrow{AB} = \big(B(x) - A(x)\big)i + \big(B(y) - A(y)\big)j + \big(B(z) - A(z)\big)k \quad (1)$$

$$\overrightarrow{AC} = \big(C(x) - A(x)\big)i + \big(C(y) - A(y)\big)j + \big(C(z) - A(z)\big)k \quad (2)$$

$$\overrightarrow{AP} = \big(P(x) - A(x)\big)i + \big(P(y) - A(y)\big)j + \big(P(z) - A(z)\big)k \quad (3)$$

or expressed in abbreviated forms:

$$\overrightarrow{AB} = a_1 i + a_2 j + a_3 k \quad (4)$$

$$\overrightarrow{AC} = b_1 i + b_2 j + b_3 k \quad (5)$$

$$\overrightarrow{AP} = p_1 i + p_2 j + p_3 k \quad (6)$$

The normal vector to the plane α can be calculated by taking the cross product of vectors $\overrightarrow{AB}$ and $\overrightarrow{AC}$:

$$\vec{n} = \overrightarrow{AB} \times \overrightarrow{AC} = \big(a_2 b_3 - a_3 b_2\big)i + \big(a_3 b_1 - a_1 b_3\big)j + \big(a_1 b_2 - a_2 b_1\big)k \quad (7)$$

or expressed in abbreviated form:

$$\vec{n} = n_1 i + n_2 j + n_3 k \quad (8)$$

The unit normal vector to the plane α can be calculated by:

$$\vec{\hat{n}} = \frac{\vec{n}}{\left|\vec{n}\right|} = \frac{n_1}{\left|\vec{n}\right|} i + \frac{n_2}{\left|\vec{n}\right|} j + \frac{n_3}{\left|\vec{n}\right|} k \tag{9}$$

where $\left|\vec{n}\right|$ is the magnitude of the normal vector and it can be calculated by:

$$\left|\vec{n}\right| = \sqrt{{n_1}^2 + {n_2}^2 + {n_3}^2} \tag{10}$$

The abbreviated form of Eq. (9) is given by:

$$\vec{\hat{n}} = \hat{n}_1 i + \hat{n}_2 j + \hat{n}_3 k \tag{11}$$

The distance from node P to the plane α, denoted as d_α in Figure 3, is defined as a scalar product of the unit normal vector $\vec{\hat{n}}$ and vector $\overrightarrow{AP}$:

$$d_\alpha = \overrightarrow{AP} \cdot \hat{n} = p_1 \hat{n}_1 + p_2 \hat{n}_2 + p_3 \hat{n}_3 \tag{12}$$

The location of Node P can be on the opposite side of the plane α when the calculated distance d_α has a negative value. It is worth indicating that the calculation of the distance d_α is used to represent distortion deviation between two aligned geometries, which is used in commercially available packages. However, for distortion compensation, the calculation of distance d_α is not sufficient to conduct a distortion compensation.

The coordinates of the projection Node O are needed in order to employ a criterion for identification to which element node P belongs. The coordinates of Node O can be obtained from the intersection between the Plane α and the line PO. The equation of the Plane α can be given by:

$$n_1 x + n_2 y + n_3 z + d = 0 \tag{13}$$

where

$$d = -\left(n_1 A(x) + n_2 A(y) + n_3 A(z)\right) \tag{14}$$

The equation of the line PO can be given by:

$$\begin{aligned} x &= P(x) + n_1 t \\ y &= P(y) + n_2 t \\ z &= P(z) + n_3 t \end{aligned} \tag{15}$$

The intersection between the Plane α and the line PO can be determined by substituting Eq. (15) into Eq. (13):

$$n_1(P(x) + n_1 t) + n_2(P(y) + n_2 t) + n_3(P(z) + n_3 t) + d = 0 \tag{16}$$

where the parameter t can be expressed by:

$$t = -\frac{n_1 P(x) + n_2 P(y) + n_3 P(z) + d}{{n_1}^2 + {n_2}^2 + {n_3}^2} \tag{17}$$

The coordinates of the node O can be obtained by substituting Eq. (17) into Eq. (15):

$$
\begin{aligned}
O(x) &= P(x) + n_1 t \\
O(y) &= P(y) + n_2 t \\
O(z) &= P(z) + n_3 t
\end{aligned} \tag{18}
$$

Once a surface criterion is employed to identify to which element Node O belongs through the search algorithm using indexing, the inverted coordinates of Node P can be calculated by:

$$
\begin{aligned}
P_{inverted}(x) &= O(x) - P(x) \\
P_{inverted}(y) &= O(y) - P(y) \\
P_{inverted}(z) &= O(z) - P(z)
\end{aligned} \tag{19}
$$

2.2 Surface method (S-method)

The criterion used to decide whether Node O is inside the triangle ABC can be obtained by the summation of the areas of the triangles AOB, AOC and BOC, which shall be equal to the area of the triangle ABC (Afazov et al., 2017a):

$$
S_{ABC} = S_{AOB} + S_{AOC} + S_{BOC} \tag{20}
$$

The area of a triangle can be defined as a half of the cross product of the two direction vectors, given by:

$$
S_{ABC} = \frac{1}{2}\left|\overrightarrow{AB} \times \overrightarrow{AC}\right| = \frac{1}{2}\sqrt{(a_2 b_3 - a_3 b_2)^2 + (a_3 b_1 - a_1 b_3)^2 + (a_1 b_2 - a_2 b_1)^2} \tag{21}
$$

Similarly, the areas of triangles AOB, AOC and BOC are given by:

$$
S_{AOB} = \frac{1}{2}\left|\overrightarrow{OA} \times \overrightarrow{OB}\right| \tag{22}
$$

$$
S_{AOC} = \frac{1}{2}\left|\overrightarrow{OA} \times \overrightarrow{OC}\right| \tag{23}
$$

$$
S_{BOC} = \frac{1}{2}\left|\overrightarrow{OB} \times \overrightarrow{OC}\right| \tag{24}
$$

To overcome exceptional conditions when a node is on the outer side of a curvature, Afazov et al. (2017a) introduced a tolerance coefficient m into Eq. (20), which was a constant value:

$$
mS_{ABC} = S_{AOB} + S_{AOC} + S_{BOC} \tag{25}
$$

In this paper, the constant value for m is replaced by the criteria in Eq. (26) which determines the minimum value for *m*:

$$
min(m) = min\left((S_{AOB} + S_{AOC} + S_{BOC})/S_{ABC}\right) \tag{26}
$$

For example, following Figure 3, the values for m are calculated for all elements of the original design surface mesh and the minimum value is used to indicate the closest element. The min(m) criterion can lead to exceptional conditions for elements far away from Node P. Therefore, a filter was introduced to exclude the elements far away by searching the elements with minimum distance *min*(d_α) and *min(m)*.

2.3 Hybrid method (H-method)

This is an improved mathematical model for distortion compensation, which is a novel element in this study and is applicable to challenging part like thin structures. The hybrid method is based on the use of an element shape function and a minimum distance to an edge in a 2D coordinate system as a criterion to identify the element to which node P belongs. Once the coordinates of Node O are calculated from Eq. 18, the element shape function is employed to decide to which element node O belongs. The shape function for a triangular 2D element requires a two-dimensional coordinate system. Therefore, a new local coordinate system is created. Figure 4 shows the coordinate system and the vectors used to define them.

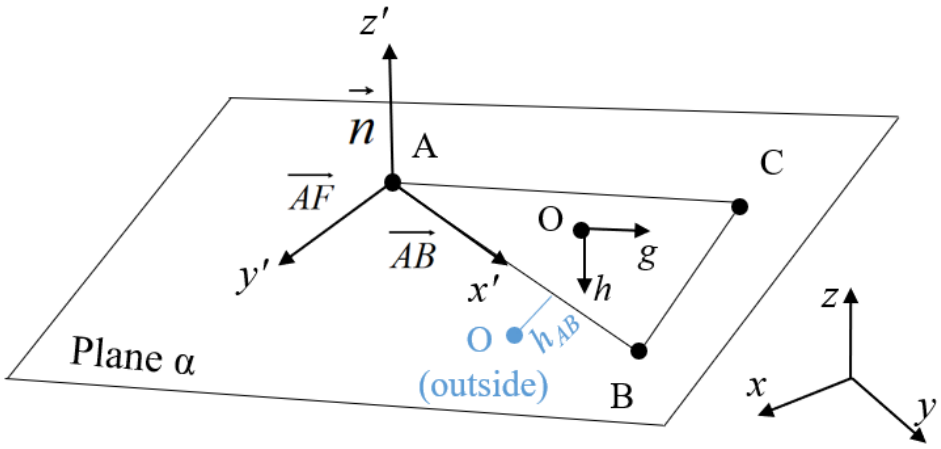

Figure 4 Coordinate systems used in the H-method. Note that the notations in blue show a scenario when node O is located outside the triangle ABC.

The normal vector $\vec{n}$ to the Plane α is used for the z' axis for the local coordinate system. Vector $\overrightarrow{AB}$ is selected as the x' axis. The unit vector of $\overrightarrow{AB}$ can be obtained by:

$$\overrightarrow{\hat{n}_{AB}} = \frac{\overrightarrow{AB}}{\left|\overrightarrow{AB}\right|} = \frac{a_1}{\left|\overrightarrow{AB}\right|} i + \frac{a_2}{\left|\overrightarrow{AB}\right|} j + \frac{a_3}{\left|\overrightarrow{AB}\right|} k \tag{27}$$

or in abbreviated form:

$$\overrightarrow{\hat{n}_{AB}} = \hat{n}_{AB_1} i + \hat{n}_{AB_2} j + \hat{n}_{AB_3} k \tag{28}$$

The cross product of the normal $\vec{n}$ and the $\overrightarrow{AB}$ vectors gives the direction vector $\overrightarrow{AF}$, which is perpendicular to the normal $\vec{n}$ and the $\overrightarrow{AB}$ vector and lies on the plane α. The direction vector $\overrightarrow{AF}$ is used for the y' axis of the local coordinate system:

$$\overrightarrow{AF} = \vec{n} \times \overrightarrow{AB} = f_1 i + f_2 j + f_3 k \tag{29}$$

The unit vector $\overrightarrow{AF}$ is given by:

$$\hat{n}_{AF} = \frac{\overrightarrow{AF}}{\left|\overrightarrow{AF}\right|} = \frac{f_1}{\left|\overrightarrow{AF}\right|} i + \frac{f_2}{\left|\overrightarrow{AF}\right|} j + \frac{f_3}{\left|\overrightarrow{AF}\right|} k \tag{30}$$

or in abbreviated form:

$$\hat{n}_{AF} = \hat{n}_{AF_1} i + \hat{n}_{AF_2} j + \hat{n}_{AF_3} k \tag{31}$$

To transfer the coordinates from the global coordinate system x-y-z to the local coordinate system x'-y'-z', the direct cosines are obtained from the unit vectors. The transformation matrix is given by:

$$\begin{bmatrix} x' \\ y' \\ z' \end{bmatrix} = \begin{bmatrix} \hat{n}_{AB_1} & \hat{n}_{AB_2} & \hat{n}_{AB_3} \\ \hat{n}_{AF_1} & \hat{n}_{AF_2} & \hat{n}_{AF_3} \\ \hat{n}_1 & \hat{n}_2 & \hat{n}_3 \end{bmatrix} \begin{bmatrix} x \\ y \\ z \end{bmatrix} \tag{32}$$

Eq. (32) is applied to the nodes A, B, C and O where the coordinates in the z' direction for the four nodes are the same. Hence, ignoring the coordinates in the z' direction, the transferred coordinates in the x' and y' are used for the shape function of the triangular element with local coordinates (g and h). The local coordinates can be obtained by solving a system of equations:

$$\begin{vmatrix} x'_O = (1-g-h)x'_A + gx'_B + hx'_C \\ y'_O = (1-g-h)y'_A + gy'_B + hy'_C \end{vmatrix} \tag{33}$$

After algebraic manipulation, Eq. (33) can be given by:

$$\begin{bmatrix} x'_O - x'_A \\ y'_O - y'_A \end{bmatrix} = \begin{bmatrix} g \\ h \end{bmatrix} \times \begin{bmatrix} x'_B - x'_A & x'_C - x'_A \\ y'_B - y'_A & y'_C - y'_A \end{bmatrix} \tag{34}$$

The local coordinates g and h are obtained by analytically solving Eq. (34) using Cramer's rule (Mittal and Kurdi-Al, 2001).

The local coordinates span a range from 0 to 1 and their sum should not exceed a value of one for any node inside the triangular element ABC. Node O is determined whether it is inside the triangular element ABC if it satisfies the criteria in Eq. (35) where the $min(d_\alpha)$ criterion is also used to filter the closest elements to node P:

$$g + h \leq 1 \; for \; min(d_\alpha) \tag{35}$$

If Eq. (35) is not satisfied for a node due to exceptional conditions where node O is not inside any element (see node O with blue notation in Figure 3), the minimum distance criterion to each edge of the element is then utilised using Eq. (36):

$$\min(h) = min(h_{AB}, h_{BC}, h_{CA}) \tag{36}$$

The *min(h)* is found by searching all element of the mesh. The heights (h) to each edge of the element are obtained as:

$$h_{AB} = \frac{\left|(y'_B - y'_A)x'_O - (x'_B - x'_A)y'_O + x'_B y'_A - y'_B x'_A\right|}{\sqrt{(x'_B - x'_A)^2 + (y'_B - y'_A)^2}} \tag{37}$$

$$h_{BC} = \frac{\left|(y'_C - y'_B)x'_O - (x'_C - x'_B)y'_O + x'_C y'_B - y'_C x'_B\right|}{\sqrt{(x'_C - x'_B)^2 + (y'_C - y'_B)^2}} \tag{38}$$

$$h_{CA} = \frac{\left|(y'_A - y'_C)x'_O - (x'_A - x'_C)y'_O + x'_A y'_C - y'_A x'_C\right|}{\sqrt{(x'_A - x'_C)^2 + (y'_A - y'_C)^2}} \tag{39}$$

3.4 Comparison of the methods

The two presented methods perform in the same way when node O is inside an element. The challenge is to identify a suitable mathematical formulation when no elements are localised. Figure 5 shows two examples. The first example represents two elements with shared nodes while the second example shows two elements with non-shared nodes. The scenario with non-shared nodes can be result of meshing, therefore, it is considered in this study. The two scenarios are common, depending on the use of a software package for generating surface meshes in STL format. Both examples show a 90° angle between the two elements representing a sharp corner. For both examples, the projection of the external nodes (see the orange and blue doted areas in Figure 5) will be outside the two elements. In this scenario, it is theoretically desirable that the external nodes between 0 to 45° belong to the top element (blue) while the nodes between 45-90° belong to the side element (orange). Two experiments were conducted to compare the S-method versus the H-method. The first experiment was on the example of the two triangular elements with shared nodes where the surface area of the top element (Sa) is changed by varying the height of the triangular element. The second experiment represents the example with the two elements with non-shared nodes where the two triangular elements are with different base size. The base of the side triangular (orange) is three times greater than the base of the top triangle (blue). The aim of these experiments was to identify which of the two methods can equally split the external nodes at 45° despite the size and shape of the triangles.

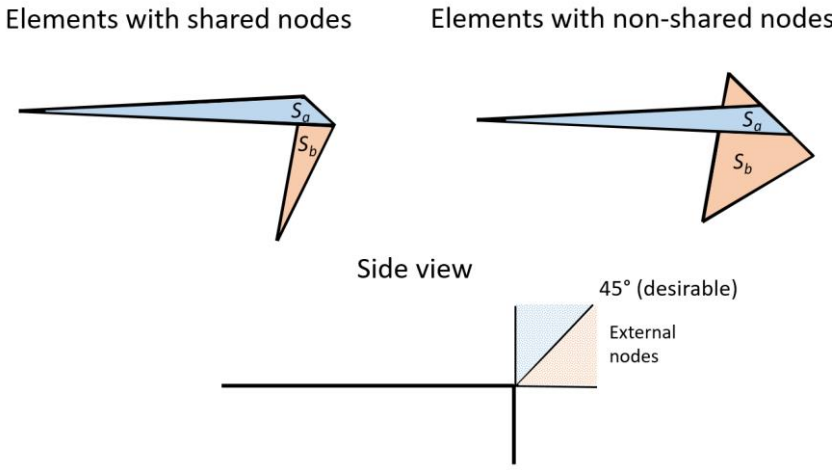

Figure 5 Design of experiment for calculation of exceptional conditions

Figure 6a and 6b show the change of the angle by changing the ratio S_a/S_b for both experiments. For $S_a/S_b = 1$, the example with shared nodes results in an angle of 45° for both methods (S-method and H-method), which is the desirable outcome. However, this is not the case for the example with non-shared nodes where at $S_a/S_b = 1$, the calculated angle is greater than 70° for the S-method. The general trend is that by increasing the S_a/S_b ratio, the angle increases for the S-method while the calculated angle with the H-method shows a constant value for the angle of 45°. It can be noted that the S-method is greatly dependent on the size of the elements as well as the base edge length for non-shared nodes. In surface meshes combining large elements with very small elements, the large elements will dominate, and the external nodes will belong to them. This is associated with accumulation of mathematical errors, particularly in small radii (sharp edges). The H-method showed that despite the element size, the desirable degree of 45° for splitting the external node was achieved

after the conducted calculations. It can be concluded that the H-method introduces less mathematical errors in calculation of distortion vectors used for distortion compensation in AM, hence this is the preferable method to conduct distortion compensation.

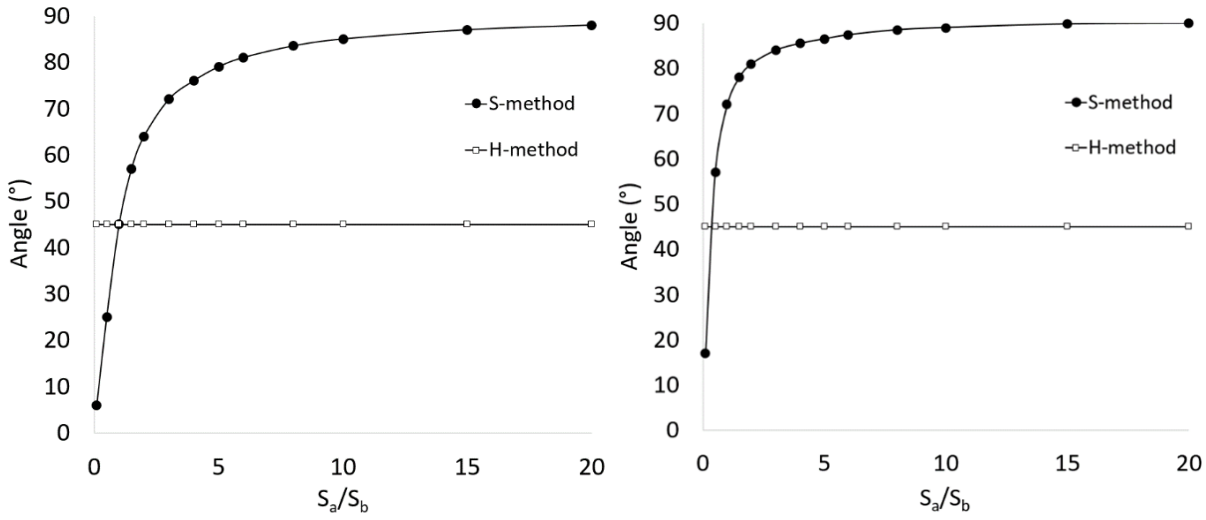

Figure 6 Comparison of mathematical methods (S-method vs H-method): (a) elements with shared nodes; (b) elements with non-shared nodes.

4. Indexed search

The presented methods need to find the element of the original designed surface mesh to which the projection of each node of the distorted surface mesh belongs. This search can be very time-consuming for large meshes if it is performed sequentially, i.e. by scanning the elements one after the other without applying any spatial criteria. In order to perform this operation efficiently, a spatial index on the original designed mesh is built, which allows to drastically reduce the time required to map a node to its associated element, compared to a sequential search. The mapping of the distorted surface mesh is also executed in parallel by splitting the mesh across multiple threads. A few different mapping techniques, including a method using elements and a method using the element shape function are implemented (Afazov et al., 2012). Spatial indexes have been widely used in diverse applications in areas such as computer graphics, computer-aided design, finite element analysis, databases and geographic information systems in order to facilitate search operations on spatial data (Samet, 2006).

A type of spatial index called grid index, where the underlying space of a mesh is partitioned into a three-dimensional orthogonal grid. Two types of grid indexes are available: one in which the grid cells are of equal size and one in which they are not. More details on the construction and use of these two indexes can be found, respectively, in (Scrimieri et al., 2014) and (Scrimieri et al., 2015). A grid index is represented by a three-dimensional array, whose size reflects that of the grid. Each grid cell is associated with a “bucket” of a fixed size that stores the elements and nodes of the cell. The association between cells and buckets is many-to-one. The creation of an index on a mesh starts with a grid of a predefined size, in which a bucket is associated with only one cell. Elements are indexed by indexing their nodes, as described in the following. As nodes are indexed and buckets get filled, the size of the grid grows, and new buckets are created.

Let us consider a grid index of size $D_1 \times D_2 \times D_3$ and let $\min_i$ and $\max_i$ be, respectively, the minimum and maximum i-th coordinate values of the nodes of the mesh. If the cells are of equal size, a node (x_1, x_2, x_3) is associated with the cell (c_1, c_2, c_3), where

$$c_i = \left\lfloor \frac{x_i - \min_i}{\max_i - \min_i} \cdot D_i \right\rfloor \tag{40}$$

for $1 \leq i \leq 3$ ($\lfloor x \rfloor$ denotes the largest integer not greater than x).

If the cells are not of equal size, an additional data structure is required, for each dimension, to specify the intervals into which the dimension is partitioned and to find the corresponding interval of the node. A binary search tree can be used for this purpose (Scrimieri et al., 2015).

The same mapping from nodes to cells is used both when indexing a node and when searching the element, a node belongs to. When searching, if the element is not found in the cell of a node, it is searched in neighbouring cells at increasing distances. This can happen if an element overlaps a cell, but the cell does not contain any of the element's nodes.

In a grid index with cells of equal size, insertion and search take constant time, but the grid refinement operation (described below) requires the splitting of all the cells to maintain the equal-size property. A grid index with non-equal size cells that uses binary search trees does not need to split all the cells during a refinement. However, insertion and search in this index take $O(\log_2 n)$ on average in each dimension, where n is the number of nodes in the tree. With both index types, the time required to create an index is negligible compared to the time saved for mapping all the nodes.

In order to create an index, there are three cases to be considered when indexing a node n in a cell $c = (i, j, k)$ associated with a bucket b, depending on whether the bucket is full or shared by multiple cells:

1. b is not full: n is added to b.
2. b is full and non-shared: The grid is refined along one dimension (cycling through the three dimensions) in a process that depends on whether the grid cells are of equal size or not:
   2.1. Equal size cells: All the grid cells are split along the chosen dimension in two cells of equal size. The size of the grid is, therefore, doubled therefore doubling the size of the grid in that dimension.
   2.2. Non-equal size cells: The grid is refined by creating a "slice". Let us suppose that the chosen dimension is the X-axis. All the cells (i, j', k') are split along the X-axis in two cells of equal size. The size of the grid is, therefore, increased by 1 in the X-axis.

   Bucket b is also split in two, with one bucket for each of the two cells resulting from the split of c, and the content of b is redistributed between the two newly created buckets, based on the associated cell to which each node belongs. For each other cell being split, the two resulting cells share the bucket of the original cell. Node n is added to the bucket of the newly created cell that contains n, if not full, otherwise the grid is refined recursively.
3. b is full and shared: b is split, creating a new non-shared bucket b', which is associated with c. The other cells associated with b are not altered. The content of b is redistributed between b and b' based on the associated cell to which each node belongs. Node n is added to b, if not full, otherwise the grid is refined recursively, as described in 2.

5. Distortion compensation – an industrial case study

A part of a manifold structure was designed with height of 210 mm and thickness of 1.5 mm. The CAD model was used to create solid supports connecting the part to the build plate. The two CAD models were meshed and sliced. The surface mesh is shown in Figure 7. It can be seen that large and small elements are used.

An EOS M290 (EOS, Krailling, Germany) L-PBF AM machine was used to manufacture the part at 3T Additive Manufacturing Ltd under an Argon atmosphere, a laser power of 190W, a laser scanning velocity of 800 mm/s, a layer thickness of 40 µm, a hatching distance of 90 µm and a stripe scanning strategy. The Inconel 718 powder from LPW Technology Inc. (LPW, Runcorn, UK) with average particle size between 15-45 µm was used for printing. The STL file was used as an input into the EOS 290 machine to build the part as shown in Figure 8.

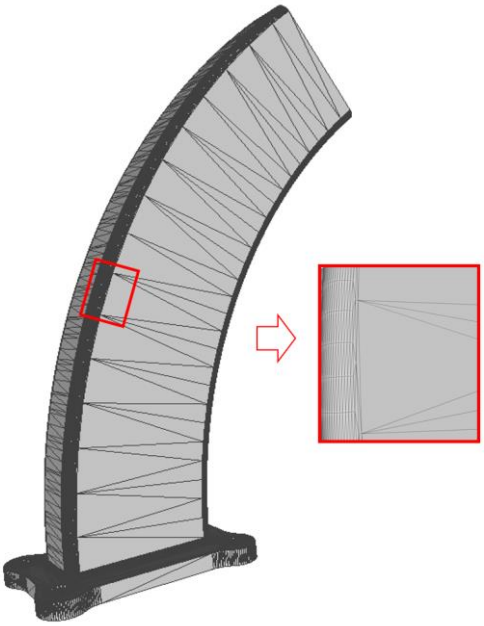

Figure 7 Surface mesh used for the build.

Figure 8 Build plate of the EOS M290 with manufactured component on it.

After the build completion, the part was optically scanned on the build plate using a blue light technology embedded in the GOM ATOS Triple Scan optical measurement system equipped with two 12-megapixel resolution cameras capable of achieving an accuracy of 10 microns (Capture 3D, 2020). This study used an approach similar to Piscopo et al. (2019) for processing the scanned data. The scanned data representing a cloud of points was converted into a surface mesh. The scanned surface mesh was aligned to the originally designed surface mesh from Figure 7 using the best-fit method implemented in the GOM 3D Inspect software (GOM 3D Inspect, 2020). The distances from the measured data to the designed geometry were calculated (see Eq. 12). The distances, also referred to as surface deviations or distortion, are shown in Figure 9. It can be seen that the measured distortion (minimum distance) is approximately ±0.36 mm. The distortion is due to residual stresses causing the thin structure to buckle as it can be seen on the side face. It should be noted that the optical scanning technology has a limitation to scan internal surfaces. Therefore, the value of 0.36 mm on the inner surface might not be representative. It should also be considered that the best-fit alignment method was applied to all nodes, which is accepted practice in industry to represent the overall distortion distribution on the entire part, but it can also show some misleading results at local level.

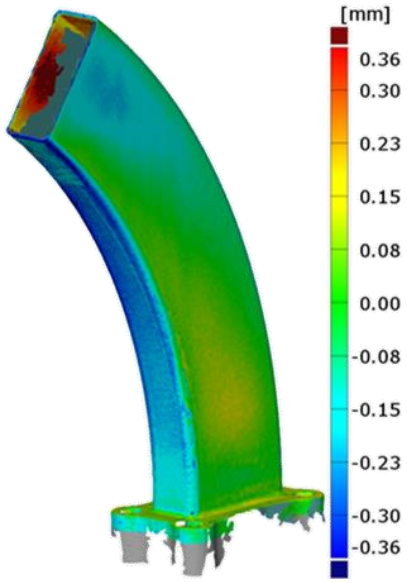

Figure 9 Calculated distortion (surface deviation) between scanned and original designed geometry

As it can be seen from Figure 9, the flat surfaces from the original geometry have distorted. This means that to capture those distortions, a refined surface mesh is needed to represent the original designed geometry in order to enable the compensation at all deformations. Figure 10 show a surface mesh with 1 mm maximum edge length. The H-method was first used to calculate the displacement vectors at the scanned points. The displacement vectors were mapped to the refined mesh in Figure 10 and the coordinates were modified to account for the compensation. Figure 11 shows the calculated distortion (minimum distance) after the compensation. Comparing Figure 9 and Figure 11, it can be seen that the distortion is inverted. This indicates that the distortion compensation has been correctly applied. It needs to be noted that the invention of the internal surfaces was done through the mapping techniques using data from the outer surfaces which have been optically scanned.

The compensated mesh was printed again on the EOS M290 machine using the same process parameters and build plate. The build was scanned using the same blue light technology and methodology. The scanned data was aligned to the original designed geometry using the best-fit method and the distortion values were computed. Figure 12 shows that the distortion has been reduced from approximately ±400 µm to ±100 µm, resulting in approximately 75% reduction. Conducting further distortion compensation iteration could further reduce the distortion below 100 µm leading to near-zero distortion in L-PBF. However, more iterations will increase the cost, but it

might be justifiable for applications requiring high precision. Conducting multiple distortion compensation iterations could increase the surface roughness too. Multiple iterations were not investigated in this study, but future research is needed to understand whether there are benefits by conducting more than one distortion compensation iterations.

The presented data-driven distortion compensation method does not have a limitation on its applicability to electron beam laser powder bed fusion (EB-PBF), DED and binder jetting. However, further research is needed to generate evidence for those processes. For instance, the DED process can introduce some challenges due to the rough surface, which might require smoothing of the scanned surface points before the mathematical calculations are applied. The binder jetting, in particular the sintering step, is associated with large deformations due to large shrinkages as well as deformation due to creep caused by the gravitational load. It should be mentioned that for complex geometries the alignment between the measured and original geometries can be a source of error generation. Another source of error generation is the measurement approach itself. The error can accumulate with each distortion compensation iteration too. Therefore, further research should be conducted to investigate whether the proposed method would work well with large deformations, as well as to understand all the associated errors with this approach for different AM processes.

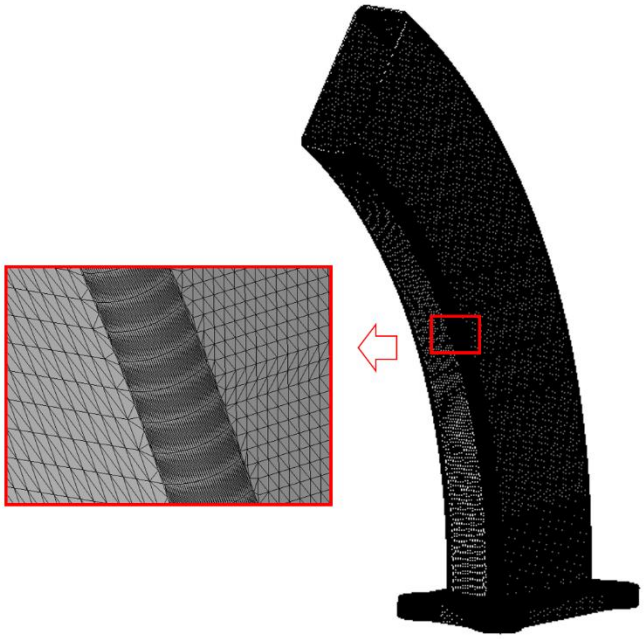

Figure 10 Refined surface mesh used for compensation

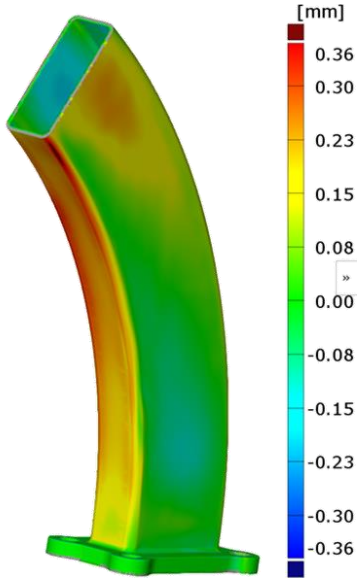

Figure 11 Calculated distortion (minimum distance) between compensated and originally designed geometry

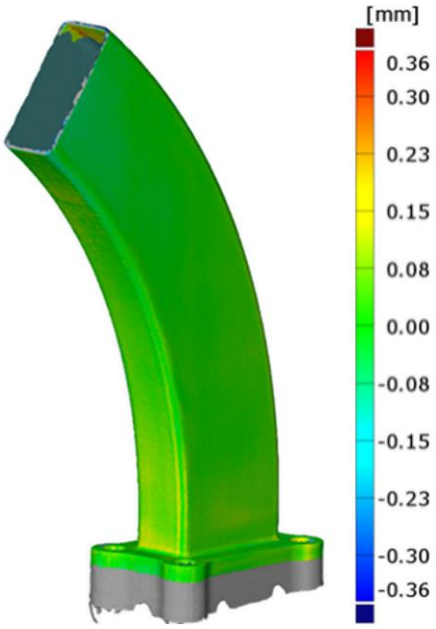

Figure 12 Comparison of distortion between build and original design after compensation.

6. Conclusions

An improved mathematical model for calculation and inversion of displacement vectors for distortion compensation was successfully developed and embedded into a digital tool.

The developed mathematical model was compared with a previously used method for distortion compensation (Afazov et al, 2017a). The results showed that the improved method is more accurate for calculating the mathematical exceptions which are observed in geometries with sharp corners or small radii as well as in transitions of small and large elements.

The mathematical model was applied to compensate distortion of an industrial Inconel 718 manifold component produced by L-PBF AM technology. The results showed distortion reduction from approximately ±400 µm to ±100 µm.

The development of a robust distortion compensation method could enable designers to use less support structures as a distortion mitigation approach, leading to reduction of manufacturing time and material waste in AM. This work paves the way for incorporation of an accurate distortion compensation method in the design workflow as a key step towards addressing challenges in industrial applications of AM.

Future research will be conducted on understanding the trade-off effect of multiple distortion compensation iterations on the dimensional accuracy, surface roughness and associated costs. Comparison of the different mathematical formulation on AM processes and industrial use cases are scoped as a future research. The accumulation of errors using this data-driven distortion compensation approach and their quantification is another research strand that needs further attention.

References

Afazov S, Becker A, Hyde T, 2012, Development of a Finite Element Data Exchange System for chain simulation of manufacturing processes, Advances in Engineering Software, 47, 104-113

Afazov S, Okioga A, Holloway A, Denmark W, Triantaphyllou A, Smith S-A, Bradley-Smith L, 2017a, A methodology for precision additive manufacturing through compensation, Precision Engineering, 50 269–274.

Afazov S, Denmark W, Lazaro Toralles B, Holloway A, Yaghi A, 2017b, Distortion prediction and compensation in selective laser melting, Additive Manufacturing, 17, 15-22

Biegler M, Elsner B, Graf B, Rethmeiera M, 2020, Geometric distortion-compensation via transient numerical simulation for directed energy deposition additive manufacturing, Science and Technology of Welding and Joining, 25 (6), 468-475

Bracco C, Giannelli C, Grobmann D, Sestini A, 2018, Adaptive fitting with THB-splines: Error analysis and industrial applications, Computer Aided Geometric Design, 62, 239-252

Capture 3D, ATOS Triple Scan - Blue Structured Light 3D Scanner for Accuracy , https://www.capture3d.com/3d-metrology-solutions/3d-scanners/atos-triple-scan, Accessed 30 December 2020

Chahal V, Taylor R, 2020, A review of geometric sensitivities in laser metal 3D printing, Virtual and Physical Prototyping, 15:2, 227-241

Cheng C, Wang A,Tsung F, 2018, A prediction and compensation scheme for in-plane shape deviation of additive manufacturing with information on process parameters, IISE Transactions, 50:5, 394-406, doi: 10.1080/24725854.2017.1402224

Eisenbarth D, Soffel F, Wegener K, 2019, Effects of direct metal deposition combines with intermediate and final milling on part distortion, Virtual and Physical Prototyping, 14:2, 130-134

Garaigordobil A, Ansola R, Vegueria E, Fernandez I, 2019, Overhang constraint for topology optimisation of self-supported compliant mechanisms considering additive manufacturing, Computer-Aided Design 109, 33-48

GOM 3D Inspect, https://www.gom.com/3d-software/gom-inspect-suite/independent-software/3d-inspection.html, Accessed 30 December 2020

Huang Q, 2015, An Analytical Foundation for Optimal Compensation of Three-Dimensional Shape Deviations in Additive Manufacturing, Journal of Manufacturing Science and Engineering 138(6), DOI: 10.1115/1.4032220

Jiang J, Xu X, Stringer J, 2018, Support structures for additive manufacturing: a review, Journal of Manufacturing and Materials Processing, 2, 64, https://doi.org/10.3390/jmmp2040064

King W, Anderson A, Hodge N, Kamath C, Khairallah S, Rubenchik A, 2015, Laser powder bed fusion additive manufacturing of metals; physics, computational, and materials challenges, Applied Physics Reviews, 2, Article 041304

Li C, Fu C, Guo Y, Fang F, 2016, A multiscale modeling approach for fast prediction of part distortion in selective laser melting, Journal of Materials Processing Technology, 229, 703–712

Liu Y, Yang Y, Wang D, 2016, A study on the residual stress during selective laser melting (SLM) of metallic powder, International Journal of Advanced manufacturing Technology, 87, 647–656.

Martinez-Pellitero S, Cuesta E, Giganto S, Barreiro J, 2018, New procedure for qualification of structured light 3D scanners using an optical feature-based gauge, Optics and Lasers in Engineering, 110, 193-206

Mittal R, Kurdi-Al A, 2001, Application of the Cramer rule in the solution of sparse systems of linear algebra equations, Journal of Computational and Applied Mathematics, 136, 1-15

Papadakis L, Loizou A, Risse J, Bremen S, Schrage J, 2014, A computational reduction model for appraising structural effects in selective lase melting manufacturing, Virtual and Physical Prototyping, 9:1, 17-25

Piscopo G, Salmi A, Atzeni E, 2019, On the quality of unsupported overhangs produced by laser powder bed fusion, International Journal of Manufacturing Research 14 (2), DOI: 10.1504/IJMR.2019.100012

Saboori A, Piscopo G, Lai M, Salmi A, Biamino S, 2020, An investigation on the effect of deposition pattern on the microstructure, mechanical properties and residual stress of 316L produced by Directed Energy Deposition, Materials Science and Engineering: A, 780, 139179

Salmi A, Piscopo G, Atzeni E, Minetola P, Iuliano L, 2018, On the effect of part orientation on stress distribution in AlSi10Mg specimens fabricated by laser powder bed fusion (L-PBF), Procedia CIRP, 67, 191 – 196

Samet H., Foundations of Multidimensional and Metric Data Structures, Morgan Kaufmann, 2006.

Scrimieri D, Afazov S, Becker A, Ratchev S, 2014, Fast mapping of finite element field variables between meshes with different densities and element types, Advances in Engineering Software, 67, 90-98

Scrimieri D, Afazov S, Ratchev S, 2015, An in-core grid index for transferring finite element data across dissimilar meshes, Advances in Engineering Software, 88, 53-62

Steuben J, Iliopoulos P, Michopoulos, 2016, Implicit slicing for functional tailored additive manufacturing, Computer-Aided Design, 77, 107-119

Thomas-Seale L, Kirkman-Brown J, Attallah M, Espino D, Shepherd, 2018, The barriers to the progression of additive manufacture: Perspectives from UK industry, International Journal of Production Economics, 198, 104-118

Xu K, Kwok T-H, Zhao Z, Chen Y, 2017, A Reverse Compensation Framework for Shape Deformation Control in Additive Manufacturing, Journal of Computing and Information Science in Engineering, doi: 10.1115/1.4034874

Yaghi A, Ayvar-Soberanis S, Moturu S, Bilkhu R, Afazov S, 2019, Design against distortion for additive manufacturing, Additive Manufacturing, 27, 224–235.